



Cite this: *RSC Adv.*, 2017, 7, 54500

One-step synthesis and upconversion luminescence properties of hierarchical $\text{In}_2\text{O}_3:\text{Yb}^{3+}, \text{Er}^{3+}$ nanorod flowers†

Yinhua Wang, Yongsheng Zhu, * Xiumei Xu,  Jinshu Huang, Zhiwen Lu and Dongfang Qiu*

$\text{In}_2\text{O}_3:\text{Yb}^{3+}, \text{Er}^{3+}$ nanorod flowers (NRFs) are prepared by a simple hydrothermal method, where sucrose was used as a ligand. The obtained $\text{In}_2\text{O}_3:\text{Yb}^{3+}, \text{Er}^{3+}$ NRFs were carefully characterized by scanning electron microscopy (SEM), power X-ray diffraction (XRD), transmission electron microscopy (TEM) and steady/transient spectroscopy. The dependence of the upconversion luminescence (UCL) of $\text{In}_2\text{O}_3:\text{Yb}^{3+}, \text{Er}^{3+}$ NRFs on morphology, Yb^{3+} concentration and excitation power was carefully discussed. It is found that the luminescence intensity ratio of the red emission to green emission (R/G) depended on the morphology and Yb^{3+} concentration, and the green emissions are dominantly resulting from a three-photon populating process with higher Yb^{3+} doping concentration. More importantly, the concentration quenching in the $\text{In}_2\text{O}_3:\text{Yb}^{3+}, \text{Er}^{3+}$ NRFs was greatly suppressed due to boundary effects, and is beneficial for lighting and photon energy conversion devices.

Received 25th September 2017

Accepted 22nd November 2017

DOI: 10.1039/c7ra10582g

rsc.li/rsc-advances

1. Introduction

Since the concept of upconversion (UC) was proposed by Auzel in 1966, upconversion nanoparticles (UCNPs) have attracted considerable attention in many fields owing to their fascinating features, because of their ability of successive absorption of several low-frequency near infrared photons and generation of one ultraviolet or visible photon.^{1–3} Furthermore, researchers found many superior advantages of UCNPs, such as multicolor emission, long lifetimes, low autofluorescence background and superior photo-stability, as well as high penetration depth, and they are widely applied in lasers, solar cells, displays, biosensors and bioimaging.^{4–10} The inorganic host is the carrier of UC and it is very important for improving the efficiency of UCL, which is affected by the morphology of UCNPs. So far, many works have been performed to synthesize different shapes of UC nanocrystals (NCs).^{11–16}

Cubic sesquioxide In_2O_3 is recognized as one of the promising host materials for both up-/down-conversion luminescence through rare earth doping.^{17–19} At present, the controllable preparation of high effective UCL of rare earth (RE) doped In_2O_3 NCs is still difficult. Several strategies have been proposed to solve these problems. For example, Chen's group synthesized Er^{3+} ions doped cubic In_2O_3 nanoparticles

via a simple solvothermal method, and firstly demonstrated its UC and downconversion emissions under 808 and 980 nm excitation, respectively.²⁰ Xu *et al.* successfully fabricated $\text{In}_2\text{O}_3:\text{RE}$ nanotubes by the electrospinning method for the first time, and the sensitivity of In_2O_3 nanotubes to H_2S were significantly improved due to the RE ions doping.²¹ Dutta's group also prepared Eu/Dy doped In_2O_3 nanoparticles by a sonochemical technique. Relatively weak Eu^{3+} emission could be detected in $\text{In}_2\text{O}_3:\text{Eu}$ nanoparticles, which is attributed to the distorted environment around the Eu ions in the In_2O_3 lattice.²² So far, although a few works on $\text{In}_2\text{O}_3:\text{RE}$ nanoparticles have been performed, the mechanism of UC processes of In_2O_3 NCs doped with Yb^{3+} , Er^{3+} ions is not fully understood. Especially, the dependence of UCL on cross relaxation, population processes, excitation power density and RE doping concentration are not clear. Therefore, it is necessary to detailedly investigate the UCL property of $\text{In}_2\text{O}_3:\text{Yb}^{3+}, \text{Er}^{3+}$ NCs.

In this article, we prepared $\text{In}_2\text{O}_3:\text{Yb}^{3+}, \text{Er}^{3+}$ hierarchical NRFs by a facile hydrothermal method using sucrose as surfactant.²³ The formation, morphology and structure of the $\text{In}_2\text{O}_3:\text{Yb}^{3+}, \text{Er}^{3+}$ NRFs were examined by SEM, TEM, and XRD. And the influence of sucrose on the hydrothermally prepared $\text{In}_2\text{O}_3:\text{Yb}^{3+}, \text{Er}^{3+}$ NRFs is further elucidated. The investigation of UCL property of the $\text{In}_2\text{O}_3:\text{Yb}^{3+}, \text{Er}^{3+}$ NRF demonstrated that the UCL intensity and R/G ratios depended on particle size, excitation power and Yb^{3+} concentration. The as-obtained $\text{In}_2\text{O}_3:\text{Yb}^{3+}, \text{Er}^{3+}$ NRFs exhibited a high effective UC emission, which is a promising candidate for display and solar cells.

College of Physics and Electronic Engineering, College of Chemistry and Pharmaceutical Engineering, Nanyang Normal University, Nanyang 473061, China.
E-mail: yongshengzhu0001@163.com; qiudf2008@163.com

† Electronic supplementary information (ESI) available. See DOI: 10.1039/c7ra10582g

2. Experimental section

2.1 Synthesis In_2O_3 nanorods flowers

All the reagents (analytical-grade purity) were used without any further purification. In the preparation of (10 mol%) Yb^{3+} , (1 mol%) Er^{3+} co-doped In_2O_3 NCs, $\text{InCl}_3 \cdot 4.5\text{H}_2\text{O}$ (266 mg), $\text{YbCl}_3 \cdot 6\text{H}_2\text{O}$ (33 mg), $\text{ErCl}_3 \cdot 6\text{H}_2\text{O}$ (3 mg), urea (15 mg) and moderate sucrose (342 mg) were dissolved in deionized water (36 mL) with adequately stirring for 30 min. In this reaction, sucrose acts as a template and linker to bind the nanoparticles, which leads to the formation of flower-like nanostructures. The presence of both sucrose and urea is a prerequisite for the formation of this porous hierarchical In_2O_3 . Then, a Teflon-lined stainless steel autoclave was used for placed for the mixture solution and placed in 160 °C oven for 12 h. After the autoclave was cooled to room temperature naturally, the result product was obtained through centrifuging the result product using deionized water and ethanol for three times, and then dried at 80 °C for 1 day. $\text{In}_2\text{O}_3:\text{Yb}^{3+},\text{Er}^{3+}$ NCs were obtained through calcining the precursor at 500 °C for 2 h. The same route is adopted for the preparation of (10 mol%) Yb^{3+} and $x\text{Er}^{3+}$ ($x = 2, 3, 5, 8$ mol%) doped In_2O_3 NCs. The preparation process of $\text{In}_2\text{O}_3:\text{Yb}^{3+},\text{Er}^{3+}$ NRFs is presented in Scheme 1.

2.2 Characterization and measurements

The SEM images were obtained on a JEOL JSM-7500F microscope operating at 15 kV. The TEM, HR-TEM and selected-area electron diffraction (SAED) images were measured on a JEOL JEM-2100 microscope operated at 200 kV. The XRD pattern was recorded on a Rigaku D/max-rA power diffractometer. The UC emission spectra and dynamics of rare earth ions were measured on an Edinburgh fluorescence spectrometer (FLS980).

3. Results and discussion

3.1 Morphology and structure characterization of $\text{In}_2\text{O}_3:\text{Yb}^{3+},\text{Er}^{3+}$ NRFs

Fig. 1 shows the XRD patterns of the calcining $\text{In}_2\text{O}_3:\text{Yb}^{3+},\text{Er}^{3+}$ products and the corresponding reference samples (REF). It can be seen that the products are the pure cubic structure according to JCPDS card no. 06-416. With space group $Ia\bar{3}$ (no. 206) and lattice parameters of $a = 10.118 \text{ \AA}$. No diffraction peaks from any other impurities were observed, indicating the high purity

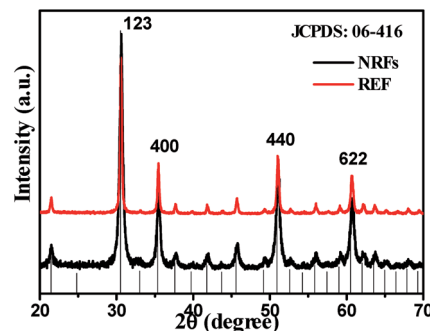


Fig. 1 X-ray diffraction patterns of as-prepared $\text{In}_2\text{O}_3:\text{Yb}^{3+},\text{Er}^{3+}$ products samples.

of the products. From the Debye–Scherer formula calculating, the average crystallite size of In_2O_3 is $\sim 15 \text{ nm}$. Fig. 2 shows the SEM images of $\text{In}_2\text{O}_3:\text{Yb}^{3+},\text{Er}^{3+}$ NCs with varying amount of sucrose. In the absence of sucrose, the product is the mixture of irregular nanocubes and flower-like nanostructures (Fig. 2a), as the reference (REF) samples. When the moderate sucrose is added, the NRFs were appeared. Fig. 2b shows the low magnification SEM image of $\text{In}_2\text{O}_3:\text{Yb}^{3+},\text{Er}^{3+}$ NRFs, demonstrated that the NRFs are high uniformity. The enlarged-magnification SEM images are presented in Fig. 2c and d, and we can see that each nanorod is uniform. Fig. 3 records the elaborate structural analysis of samples using TEM. In Fig. 3a, it can be seen that each nanorod of NRFs is homogenous, and the size of these nanorods is $\sim 100 \text{ nm}$ in diameter and $\sim 1 \mu\text{m}$ in length (Fig. 3b). From the TEM images, we can deduce that the NRFs are self-assembled by many single nanorods. The inter-planar spacing is $\sim 0.292 \text{ nm}$ through measuring the lattice fringes (Fig. 3c), matching with the distance of the (2 2 2) plane of the cubic In_2O_3 crystal. The SAED pattern of the $\text{In}_2\text{O}_3:\text{Yb}^{3+},\text{Er}^{3+}$ NRFs (Fig. 3d) confirms that the obtained products are polycrystalline in structure. In order to further determine the structure and dopant concentrations of $\text{In}_2\text{O}_3:\text{Yb}^{3+},\text{Er}^{3+}$ NRFs, the energy-dispersive X-ray (EDX) analysis of $\text{In}_2\text{O}_3:(10 \text{ mol}\%)$

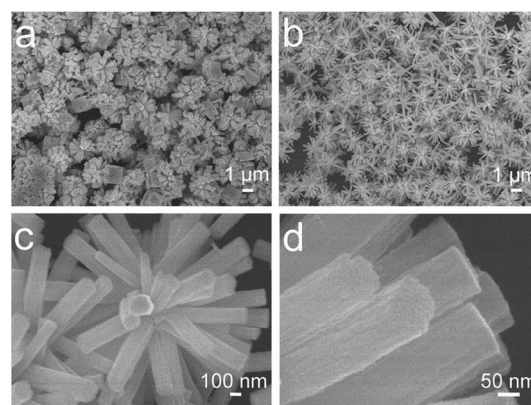
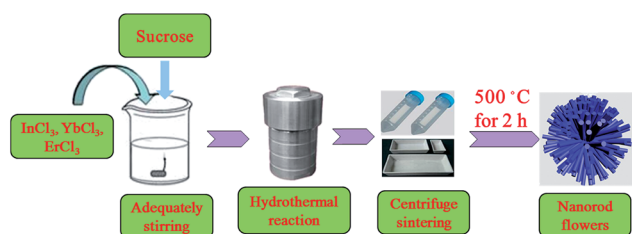


Fig. 2 (a) SEM image of the $\text{In}_2\text{O}_3:\text{Yb}^{3+},\text{Er}^{3+}$ nanocrystals prepared without sucrose, SEM images of the as-synthesized $\text{In}_2\text{O}_3:\text{Yb}^{3+},\text{Er}^{3+}$ NRFs (b) a panoramic and (c) an enlarged of a part of samples. (d) High-magnification SEM image of $\text{In}_2\text{O}_3:\text{Yb}^{3+},\text{Er}^{3+}$ nanorod.



Scheme 1 Schematic illustration for the synthesis of $\text{In}_2\text{O}_3:\text{Yb}^{3+},\text{Er}^{3+}$ NRFs.

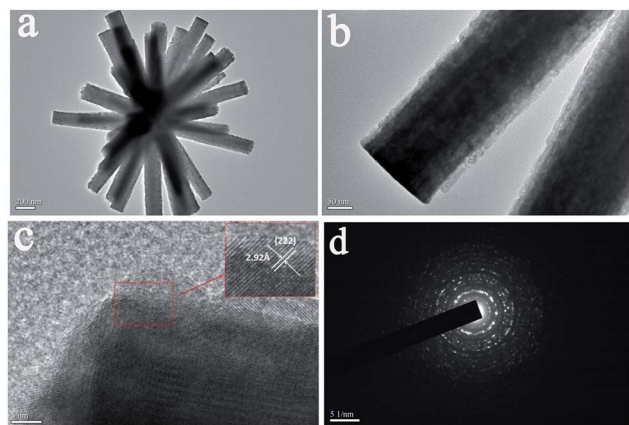


Fig. 3 Typical TEM images of $\text{In}_2\text{O}_3:\text{Yb}^{3+},\text{Er}^{3+}$ NRFs (a) and single nanorod (b), HR-TEM image of $\text{In}_2\text{O}_3:\text{Yb}^{3+},\text{Er}^{3+}$ NRFs (c), the corresponding SAED pattern (d).

$\text{Yb}^{3+},(2 \text{ mol}\%)\text{Er}^{3+}$ NRFs is measured in Fig. S1.† It shows the presence of In, Yb, Er and O element. Furthermore, the spectrum confirms that the mole ratio of Yb and Er in the NRFs is 8.47 and 1.7, respectively. According to this measuring result, we can deduce that the exact doping concentration of Er^{3+} ions is 0.85 mol%, 2.55 mol%, 4.24 mol%, 6.79 mol% in $\text{In}_2\text{O}_3:(10 \text{ mol}\%)\text{Yb}^{3+},x\text{Er}^{3+}$ ($x = 1, 3, 5, 8 \text{ mol}\%$) NRFs.

3.2 Effect of morphology, Yb^{3+} concentration and excitation power on UCL

The typical UCL spectra of $\text{In}_2\text{O}_3:\text{Yb}^{3+},(1 \text{ mol}\%)\text{Er}^{3+}$ REF and NRFs samples were investigated (Fig. 4). In the two samples, the $^4\text{F}_{3/2}-^4\text{I}_{15/2}$ (blue), $^2\text{H}_{11/2}$, $^4\text{S}_{3/2}-^4\text{I}_{15/2}$ (green) and $^4\text{F}_{9/2}-^4\text{I}_{15/2}$ (red) transitions can be clearly identified. The intensity ratio of the red ($^4\text{F}_{9/2}-^4\text{I}_{15/2}$) emission to the green ($^2\text{H}_{11/2}$, $^4\text{S}_{3/2}-^4\text{I}_{15/2}$) emissions (R/G) in $\text{In}_2\text{O}_3:\text{Yb}^{3+},\text{Er}^{3+}$ NRFs is higher than that in REF sample. The UCL property could be influenced by the following three factors: the nanocrystal size, crystallinity, and morphology. From the XRD and SEM analysis, we can deduce that the crystallinity and the size of $\text{In}_2\text{O}_3:\text{Yb}^{3+},\text{Er}^{3+}$ NRFs and REF samples are both nearly same, indicating that the effect of the size and crystallinity might not be the dominant reason to

the change of R/G ratio. The remarkable change in the R/G ratio between $\text{In}_2\text{O}_3:\text{Yb}^{3+},\text{Er}^{3+}$ NRFs and REF samples could be attributed to the change of morphology. The $\text{In}_2\text{O}_3:\text{Yb}^{3+},\text{Er}^{3+}$ NRFs constituted with dispersive nanorods has a large specific surface area, which introduced more surface ligands and surface defects. These groups and defects can bridge some non-radiative relaxation channels, such as $^4\text{I}_{13/2}-^4\text{I}_{11/2}$ and $^4\text{S}_{3/2}-^4\text{F}_{9/2}$, favoring the generation of the $^4\text{F}_{9/2}-^4\text{I}_{15/2}$ red emission. In order to verify the conclusion, the $\text{In}_2\text{O}_3:(10 \text{ mol}\%)\text{Yb}^{3+},(1 \text{ mol}\%)\text{Er}^{3+}$ power was prepared by the sol-gel method, the UCL spectra of $\text{In}_2\text{O}_3:\text{Yb}^{3+},\text{Er}^{3+}$ power (the size $> 10 \mu\text{m}$) was measured under 980 nm excitation, shown in Fig. S2.† We can find that the R/G in the power is also dramatically lower than that in $\text{In}_2\text{O}_3:\text{Yb}^{3+},\text{Er}^{3+}$ NRFs. The integral intensity of UCL for $\text{In}_2\text{O}_3:\text{Yb}^{3+},\text{Er}^{3+}$ NRFs is lower than REF sample. Then the UCL intensity of $\text{In}_2\text{O}_3:\text{Yb}^{3+},\text{Er}^{3+}$ NRFs exceeds REF samples with further increase the doping concentration of Er^{3+} (shown in the insert of Fig. 4). This phenomenon is known as concentration quenching and quite common in RE-doping NCs, which is due to an energy migration process among the same type of RE ions.²⁴ In $\text{In}_2\text{O}_3:\text{Yb}^{3+},\text{Er}^{3+}$ NRFs, the nanorod is only $\sim 100 \text{ nm}$ and dispersive each other, which can be clearly recognized by HR-TEM images (as shown in Fig. 3). The boundary effects in other traditional NCs would be unavoidably occurred. For example, in the $\text{Y}_2\text{O}_3:\text{Eu}^{3+},\text{Y}_2\text{SiO}_5:\text{Eu}^{3+}$, and $\text{LaPO}_4:\text{Ce}^{3+},\text{Tb}^{3+}$ inverse opal photonic crystals,^{25–27} the quenching concentration of the RE emission increases more than relative to the corresponding bulk phosphors. In other words, the concentration quenching was suppressed considerably due to the boundary effects.

To further understand the UCL mechanism, the UCL dynamics of $^4\text{F}_{9/2}-^4\text{I}_{15/2}$ transition of $\text{In}_2\text{O}_3:\text{Yb}^{3+},(1 \text{ mol}\%)\text{Er}^{3+}$ REF and NRFs were measured (Fig. 5), and all the decay curves of Er^{3+} ions were fitted by the double-exponential function.²⁸ From the lifetime constants, we can concluded that: (1) in the lower doped concentration of Er^{3+} ions, the lifetimes in REF samples are longer than that in $\text{In}_2\text{O}_3:\text{Yb}^{3+},\text{Er}^{3+}$ NRFs. As we known, the decay time constant is the reverse of the non-radiative and radiative decay rates. The non-radiative decay rate is significantly affected by the large phonon groups in the surface, crystal phase, lattice defect state and phonon energy. In $\text{In}_2\text{O}_3:\text{Yb}^{3+},\text{Er}^{3+}$ NRFs, the non-radiative channels nearby Er^{3+}

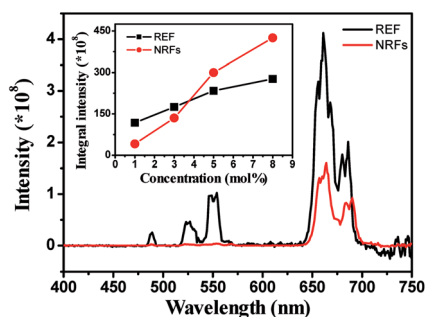


Fig. 4 Emission spectra of $\text{In}_2\text{O}_3:\text{Yb}^{3+},\text{Er}^{3+}$ in REF and NRFs under 980 nm excitation. Insert: dependence of integral intensity on Er^{3+} ions concentration of $\text{In}_2\text{O}_3:\text{Yb}^{3+},\text{Er}^{3+}$ REF and NRFs.

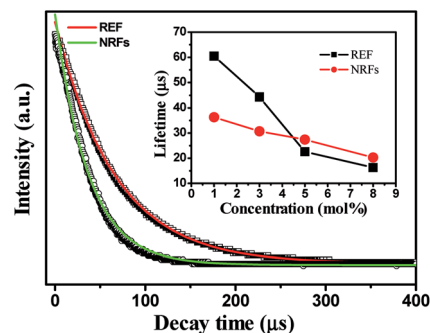


Fig. 5 The luminescent decay dynamics of the $^4\text{F}_{9/2}-^4\text{I}_{15/2}$ transition at 660 nm in $\text{In}_2\text{O}_3:\text{Yb}^{3+},\text{Er}^{3+}$ REF and NRFs. Insert: dependence of lifetimes on Er^{3+} concentration of $\text{In}_2\text{O}_3:\text{Yb}^{3+},\text{Er}^{3+}$ REF and NRFs.



ions, such as lattice defect states/surface large phonon bands would be increased due to the increasing of the volume to surface ratio.²⁹ (2) In the $\text{In}_2\text{O}_3:\text{Yb}^{3+},\text{Er}^{3+}$ NRFs, the lifetime constants decrease gradually with the increasing of Er^{3+} concentration compared to those of REF samples (as shown in the insert of Fig. 5), implying that the concentration quenching in the NRFs are suppressed. In the traditional $\text{In}_2\text{O}_3:\text{Yb}^{3+},\text{Er}^{3+}$ phosphors, the long-range resonant energy transfer (ET) processes among Er^{3+} ions are very severe. Inevitably, luminescent quenching could occur because of the ET from Er^{3+} ions to defect states, which is dependent on doped concentrations. In the $\text{In}_2\text{O}_3:\text{Yb}^{3+},\text{Er}^{3+}$ NRFs, these ET process should be restrained largely due to the structure of NRFs, because the size of each nanorod is ~ 100 nm and the nanorods are dispersive. In this case, the ET among Er^{3+} ions can only happen within one nanorod, then, the photons will be scattered into the air instead of capturing by the defect states.

Fig. 6 shows the Yb^{3+} concentration dependent UCL spectra of the $\text{In}_2\text{O}_3:\text{Yb}^{3+},\text{Er}^{3+}$ NRFs. From the spectra analysis of Fig. 6, the integral intensity of red emission gradually increased, whereas that of green emissions diminished gradually as the Yb^{3+} concentration increases. The emission spectra of the $\text{In}_2\text{O}_3:\text{Yb}^{3+},\text{Er}^{3+}$ NRFs at different excitation powers were also measured (Fig. 7). We can found that the red emission is dominant in the low excitation power, and the R/G ratio is as high as ~ 35 when the excitation power is 330 mW. The blue and green emissions increased gradually with increasing of excitation power. The R/G ratio *versus* excitation power is shown in the insert of Fig. 7, it is clear seen that the R/G ratios decreased with increasing of excitation power.

The \ln - \ln plots of the integral intensity *versus* excitation power for the red and green emissions of $\text{In}_2\text{O}_3:(15 \text{ mol}\%)\text{Yb}^{3+},x\text{Er}^{3+}$ ($x = 1, 3, 5, 8 \text{ mol}\%$) NRFs are investigated (Fig. 8). As is well known, the visible output power intensity (I_v) will be proportional to power (n) of the infrared excitation (I_{IR}) power if the saturation effect can be neglected:³⁰ $I_v \propto I_{\text{IR}}^n$, where n is the number of IR photons absorbed per visible photon emitted. The slopes n are determined to be 2.68, 2.62, 2.65, 2.4 for $^2\text{H}_{11/2}-^4\text{I}_{15/2}$ transition, 2.87, 2.62, 2.73, 2.02 for $^4\text{S}_{3/2}-^4\text{I}_{15/2}$ transition and 1.17, 1.71, 1.79, 1.86 for $^4\text{F}_{9/2}-^4\text{I}_{15/2}$ transition in the $\text{In}_2\text{O}_3:\text{Yb}^{3+},\text{Er}^{3+}$ NRFs at different Er^{3+} ions concentration of 1 mol%, 3 mol%, 5 mol% and

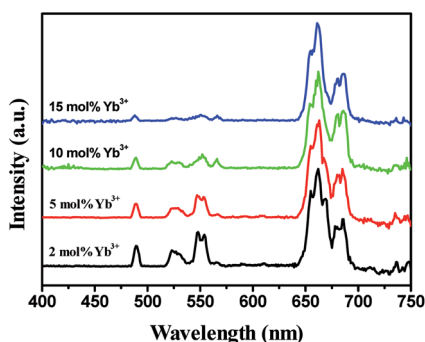


Fig. 6 UCL spectra in the $\text{In}_2\text{O}_3:\text{Yb}^{3+},(1 \text{ mol}\%)\text{Er}^{3+}$ NRFs with different concentration of Yb^{3+} .

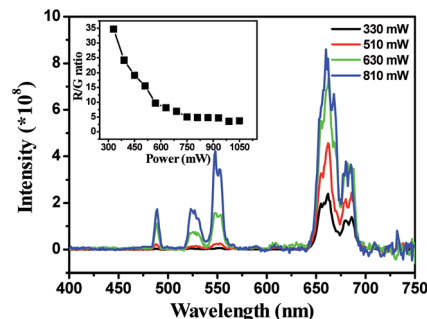


Fig. 7 Power-dependent UC emission spectra of $\text{In}_2\text{O}_3:(15 \text{ mol}\%)\text{Yb}^{3+},(1 \text{ mol}\%)\text{Er}^{3+}$ NRFs under 980 nm excitation. Insert: the R/G ratios of $\text{In}_2\text{O}_3:\text{Yb}^{3+},\text{Er}^{3+}$ NRFs *versus* excitation power.

8 mol%, respectively. We can see that the slopes n are >2 for the green emissions and >1 for the red emission of Er^{3+} . Thus the $^2\text{H}_{11/2}/^4\text{S}_{3/2}$ levels are populating through three photons processes, and the $^4\text{F}_{9/2}$ level is populating through two-photons ET processes for all the $\text{In}_2\text{O}_3:\text{Yb}^{3+},\text{Er}^{3+}$ NRFs. As far as we know, the three-photon populating phenomenon for the $^2\text{H}_{11/2}/^4\text{S}_{3/2}$ levels is few reported in $\text{Er}^{3+}/\text{Yb}^{3+}$ codoped materials.

3.3 The mechanisms of UC population and luminescence processes in $\text{In}_2\text{O}_3:\text{Yb}^{3+},\text{Er}^{3+}$ NRFs

The population mechanisms of $^4\text{S}_{3/2}$ and $^4\text{F}_{9/2}$ levels in $\text{In}_2\text{O}_3:\text{Yb}^{3+},\text{Er}^{3+}$ NRFs are quite different to other UC nanocrystals from the above analysis. Fig. 9 presents UC population and emission diagram of the $\text{Er}^{3+}/\text{Yb}^{3+}$ doping system under 980 nm excitation. The $^4\text{I}_{11/2}$ level is populated by the electrons on the ground state $^4\text{I}_{15/2}$ *via* ET of neighboring Yb^{3+} ions. Subsequently, the $^4\text{I}_{13/2}$ level is populating through the non-radiative relaxation process of $^4\text{I}_{11/2}-^4\text{I}_{13/2}$ *via* the assistance of large phonon groups, which is widely existed in NCs prepared *via* the hydrothermal method.³¹ In the second-step, the UC population of $^4\text{I}_{11/2}-^4\text{F}_{7/2}$ and $^4\text{I}_{13/2}-^4\text{F}_{9/2}$ occurred *via* ET and excited-state absorption, generating the red emission ($^4\text{F}_{9/2}-^4\text{I}_{15/2}$). The cross relaxation of $^4\text{F}_{7/2} + ^4\text{I}_{11/2} \rightarrow ^4\text{F}_{9/2} + ^4\text{F}_{9/2}$ is significant for populating the $^4\text{F}_{9/2}$ level, when the excitation power or the Yb^{3+} concentration is sufficiently high. Then the Yb^{3+} concentration is lower in $\text{In}_2\text{O}_3:\text{Yb}^{3+},\text{Er}^{3+}$ NRFs, the electrons in $^4\text{F}_{7/2}$ level is also populating $^2\text{H}_{11/2}/^4\text{S}_{3/2}$ levels through non-radiative relaxation, generating $^2\text{H}_{11/2}$, $^4\text{S}_{3/2}-^4\text{I}_{15/2}$ transitions. For populating $^4\text{S}_{3/2}/^2\text{H}_{11/2}$ levels, the non-radiative relaxation of $^4\text{I}_{11/2}-^4\text{I}_{13/2}$ is involved. The energy gap (ΔE) is $\sim 3700 \text{ cm}^{-1}$ between $^4\text{I}_{11/2}$ and $^4\text{I}_{13/2}$ level. For the bulk host, the phonon energy ($\hbar\omega$) is $\sim 580 \text{ cm}^{-1}$,³² the matching of non-radiative relaxation of $^4\text{I}_{11/2}-^4\text{I}_{13/2}$ requires at least seven host phonons, so this process is hardly happened. In $\text{In}_2\text{O}_3:\text{Yb}^{3+},\text{Er}^{3+}$ NRFs prepared by the hydrothermal method, the large phonon groups are involved due to surfactant or surface defects, so the non-radiative relaxation of $^4\text{I}_{11/2}-^4\text{I}_{13/2}$ can be bridged more effectively *via* the assistance of the large phonon group than the non-radiative relaxation of $^4\text{I}_{13/2}-^4\text{I}_{15/2}$. Therefore, the linear decay is dominant for the $^4\text{I}_{11/2}$ level, because the effective non-radiative relaxation of $^4\text{I}_{11/2}-^4\text{I}_{13/2}$ increases the linear decay processes, which leads the population



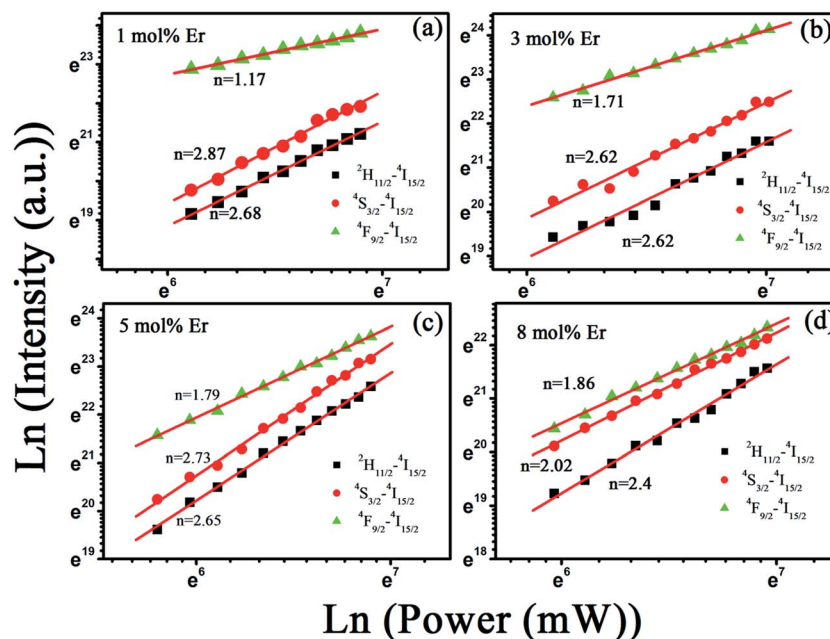


Fig. 8 Plot (ln–ln) of emission intensity versus excitation power in $\text{In}_2\text{O}_3:(15 \text{ mol}\%)\text{Yb}^{3+}, (1 \text{ mol}\%)\text{Er}^{3+}$ NRFs prepared at different concentration of Er^{3+} ions.

of $^4\text{I}_{13/2}-^4\text{F}_{9/2}$ to be more effective. This is a main reason for increasing the R/G ratio in $\text{In}_2\text{O}_3:\text{Yb}^{3+}, \text{Er}^{3+}$ NRFs.

The relation of R/G ratio and Yb^{3+} concentration can be explained below, the population of $^4\text{F}_{9/2}$ level is mainly originated from ET upconversion processes. The ET transfer from Yb^{3+} ions to Er^{3+} ions could be increased with the increase of Yb^{3+} concentration, thus the red emission ($^4\text{F}_{9/2}-^4\text{I}_{15/2}$) was accelerated because of an increase of the ET process. The quenching of green emission with the increasing Yb^{3+} concentration is due to the reversed ET from Er^{3+} to Yb^{3+} ions ($^4\text{S}_{3/2}(\text{Er}^{3+}) + ^2\text{F}_{7/2}(\text{Yb}^{3+}) \rightarrow ^4\text{I}_{13/2}(\text{Er}^{3+}) + ^2\text{F}_{5/2}(\text{Yb}^{3+})$), which leads to the depopulation of the $^4\text{S}_{3/2}$ level. As we all known, the phonon energy of In_2O_3 is larger than that of Yb_2O_3 , which may lead to the increase of nonradiative relaxation. However, all the

emissions (including red emission and green emission) will be quenching due to the nonradiative relaxation. The quenching of the green emissions is mainly attributed to the reversed ET from Yb^{3+} ions to Er^{3+} ions, which can be confirmed by the fluorescence decay of $^4\text{S}_{3/2}$ level. Finally, the power-dependent UCL in $\text{In}_2\text{O}_3:\text{Yb}^{3+}, \text{Er}^{3+}$ NRFs can be well explained. The three-photon population processes $^4\text{F}_{9/2}-^4\text{G}_{11/2}$ become more effective with the increasing of excitation power, leading the depopulation of the $^4\text{F}_{9/2}$ level and the population enhancement of $^4\text{G}_{11/2}$. The populations for $^4\text{F}_{3/2}$ and $^4\text{S}_{3/2}/^2\text{H}_{11/2}$ levels also increase due to multi-phonon relaxation, so the R/G ratio decreases as the excitation power increases.

4. Conclusion

$\text{In}_2\text{O}_3:\text{Yb}^{3+}, \text{Er}^{3+}$ NRFs has been successfully prepared by a simple hydrothermal method combined with a succedent calcining process. It is also found that in $\text{In}_2\text{O}_3:\text{Yb}^{3+}, \text{Er}^{3+}$ NRFs, the concentration quenching is dramatically suppressed. The R/G ratio changed depending on the NP morphology, Yb^{3+} concentration and the excitation power. The green emissions are mainly originated from three-photon excitation in $\text{In}_2\text{O}_3:\text{Yb}^{3+}, \text{Er}^{3+}$ NRFs with higher Yb^{3+} concentration, which is different from other substrate materials. The $\text{In}_2\text{O}_3:\text{Yb}^{3+}, \text{Er}^{3+}$ NRFs are potential candidate for the application of lighting and solar cell.

Conflicts of interest

The authors declare no competing financial interest.

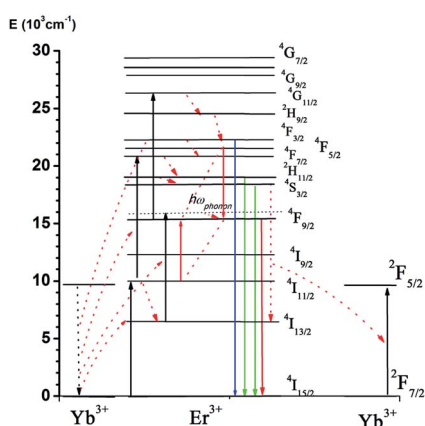


Fig. 9 Energy level diagram of $\text{In}_2\text{O}_3:\text{Yb}^{3+}, \text{Er}^{3+}$ NRFs and UCL processes under 980 nm excitation.



Acknowledgements

This work was supported by National Natural Science Foundation of China (Grant no. 11504188, 11504131, 51374132, 21571109), Natural Science Foundation of Henan Province (Grant no. U1504626).

References

- 1 F. Auzel, *Chem. Rev.*, 2004, **104**, 139–174.
- 2 P. P. Lei, R. An, S. Yao, Q. S. Wang, L. L. Dong, X. Xu, K. M. Du, J. Feng and H. J. Zhang, *Adv. Mater.*, 2017, **29**, 1700505.
- 3 M. Haase and H. Schafer, *Angew. Chem., Int. Ed.*, 2011, **50**, 5808–5829.
- 4 X. Chen, Y. S. Zhu, D. L. Zhou, W. Xu, J. Y. Zhu, G. C. Pan, Z. Yin, H. Wang, S. B. Cui and H. W. Song, *J. Mater. Chem. C*, 2017, **5**, 2451–2458.
- 5 T. Hinamoto, H. Takashina, H. Sugimoto and M. Fujii, *J. Phys. Chem. C*, 2017, **121**, 8077–8083.
- 6 I. Hyppänen, N. Höysniemi, R. Arppe, M. Schäferling and T. Soukka, *J. Phys. Chem. C*, 2017, **121**, 6924–6929.
- 7 C. Yao, P. Y. Wang, R. Wang, L. Zhou, A. M. El-Toni, Y. Q. Lu, X. M. Li and F. Zhang, *Anal. Chem.*, 2016, **88**, 1930–1936.
- 8 Y. M. Li, Y. M. Li, R. Wang, Y. L. Xu and W. Zheng, *New J. Chem.*, 2017, **41**, 7116–7122.
- 9 S. Y. Han, A. Samanta, X. J. Xie, L. Huang, J. J. Peng, S. J. Park, D. B. L. Teh, Y. Choi, Y. T. Chang, A. H. All, Y. M. Yang, B. G. Xing and X. G. Liu, *Adv. Mater.*, 2017, **29**, 1700244.
- 10 Y. Liu, Q. Q. Su, M. Chen, Y. Dong, Y. B. Shi, W. Feng, Z. Y. Wu and F. Y. Li, *Adv. Mater.*, 2016, **28**, 6625–6630.
- 11 Y. S. Zhu, W. Xu, S. B. Cui, M. Liu, C. Lu, H. W. Song and D. H. Kim, *J. Mater. Chem. C*, 2016, **4**, 331–339.
- 12 J. Wang, H. W. Song, W. Xu, B. Dong, S. Xu, B. T. Chen, W. Yu and S. Zhang, *Nanoscale*, 2013, **5**, 3412–3420.
- 13 J. H. Kang, S. S. Lee, J. Guerrero, A. Fernandez-Nieves, S. H. Kim and E. Reichmanis, *Adv. Mater.*, 2017, **29**, 1606830.
- 14 Y. Luo, S. N. Du, W. Zhang, Z. F. Liao, F. Zuo and S. T. Yang, *RSC Adv.*, 2017, **7**, 37929–37937.
- 15 D. M. Yang, Y. L. Dai, P. G. Ma, X. J. Kang, Z. Y. Cheng, C. X. Li and J. Lin, *Chem.–Eur. J.*, 2013, **19**, 2685–2694.
- 16 S. W. Hao, G. Y. Chen, C. H. Yang, W. Shao, W. Wei, Y. Liu and P. N. Prasad, *Nanoscale*, 2017, **9**, 10633–10638.
- 17 Y. G. Choi, S. M. Yu and W. J. Chung, *Chem. Phys. Lett.*, 2008, **461**, 290–293.
- 18 A. Podhorodecki, R. Kudrawiec, J. Misiewicz, N. V. Gaponenko and D. A. Tsykrunov, *Opt. Mater.*, 2006, **28**, 685–687.
- 19 H. K. Kim, C. C. Li, G. Nykolak and P. C. Becker, *J. Appl. Phys.*, 1994, **76**, 8209–8211.
- 20 Q. B. Xiao, H. M. Zhu, D. T. Tu, E. Ma and X. Y. Chen, *J. Phys. Chem. C*, 2013, **117**, 10834–10841.
- 21 L. Xu, B. Dong, Y. Wang, X. Bai, J. S. Chen, Q. Liu and H. W. Song, *J. Phys. Chem. C*, 2010, **114**, 9089–9095.
- 22 D. P. Dutta, V. Sudarsan, P. Srinivasu, A. Vinu and A. K. Tyagi, *J. Phys. Chem. C*, 2008, **112**, 6781–6785.
- 23 X. M. Xu, D. W. Wang, W. B. Wang, P. Sun, J. Ma, X. S. Liang, Y. F. Sun, Y. G. Ma and G. Y. Lu, *Sens. Actuators, B*, 2012, **171**, 1066–1072.
- 24 Y. Ruan, Q. B. Xiao, W. Q. Luo, R. F. Li and X. Y. Chen, *Nanotechnology*, 2011, **22**, 275701.
- 25 J. L. Ferrari, A. M. Pires and M. R. Davolos, *Mater. Chem. Phys.*, 2009, **113**, 587–590.
- 26 P. Ghosh, S. Sadhu and A. Patra, *Phys. Chem. Chem. Phys.*, 2006, **8**, 3342–3348.
- 27 Y. S. Zhu, Z. P. Sun, Z. Yin, H. W. Song, W. Xu, Y. F. Wang, L. G. Zhang and H. Z. Zhang, *Dalton Trans.*, 2013, **42**, 8049–8057.
- 28 M. Yu, J. Lin and J. Fang, *Chem. Mater.*, 2005, **17**, 1783–1791.
- 29 X. Bai, H. W. Song, G. H. Pan, Y. Q. Lei, T. Wang, X. G. Ren, S. Z. Lu, B. Dong, Q. L. Dai and L. B. Fan, *J. Phys. Chem. C*, 2007, **111**, 13611–13617.
- 30 N. Niu, P. P. Yang, F. He, X. Zhang, S. L. Gai, C. X. Li and J. Lin, *J. Mater. Chem.*, 2012, **22**, 10889.
- 31 J. A. Capobianco, F. Vetrone, T. Alesio, G. Tessari and M. Bettinelli, *Phys. Chem. Chem. Phys.*, 2000, **2**, 3203–3207.
- 32 A. Raza, O. P. Agnihotri and B. K. Gupta, *J. Phys. D: Appl. Phys.*, 1977, **10**, 1871–1876.

